## Surface Topography: Metrology and Properties



RECEIVED 6 March 2021

6 March 202

REVISED 19 April 2021

ACCEPTED FOR PUBLICATION 13 May 2021

PUBLISHED 28 May 2021

#### **PAPER**

# Microstructural and topographical characterization of the pack cemented aluminide coating applied on Inconel-600

Sina Mahini<sup>1</sup>, Shahin Khameneh Asl<sup>1</sup>, Taher Rabizadeh<sup>1</sup> and Hossein Aghajani<sup>2</sup>

- Department of Materials Engineering, Faculty of Mechanical Engineering, University of Tabriz, 51666-16471, Tabriz, Iran
- <sup>2</sup> School of Materials and Metallurgical Engineering, Iran University of Science and Technology, Narmak, Tehran, Iran

E-mail: t.rabizadeh@tabrizu.ac.ir

Keywords: pack cementation, aluminide coating, roughness, scanning electron microscopy, x-ray diffraction, vickers microhardness measurement

#### Abstract

In this research, the pack cementation method was employed to apply a uniform aluminide coating on a substrate of nickel-based superalloy. The obtained intermetallic coating was synthesized using a pack containing 18Al–80Al<sub>2</sub>O<sub>3</sub>–2NH<sub>4</sub>Cl (wt.%) as the main deposition source, an inert filler, and an activator, respectively. The surface morphology and topography, cross-sectional microstructure, the elemental and phase composition, microhardness of the synthesized aluminide coating were studied using atomic force microscopy (AFM), optical microscopy (OM), scanning electron microscopy (SEM), energy-dispersive spectroscopy (EDS), x-ray diffraction (XRD), and Vickers microhardness indenter as the characterization techniques. According to the 3D topography results, the average surface roughness of the Inconel-600 substrate was about 2.446  $\,\pm\,$  0.239 nm compared to  $43.558 \pm 3.876$  nm measured for the produced aluminide coating. Additionally, the synthesized coating consisted of NiAl and Ni<sub>2</sub>Al<sub>3</sub> as major phases considering the XRD spectrum. It is also observed that the deposited aluminide coating had a three-layer structure including an outer layer, an inner layer, and a diffusion zone. The Vickers microhardness measurements indicated a significant increase in the microhardness of the substrate (from 185.6  $\pm$  15.8 Hy to 1130.4  $\pm$  42.5 Hy) after applying the aluminide coating. Moreover, the microstructural variations across the deposited aluminide coating led to different microhardness values obtained for each layer. The highest microhardness was observed in the coating diffusion zone, whereas the lowest value belonged to the outer layer.

## 1. Introduction

Nickel-based superalloys are high-performance alloys used in different industries such as oil and gas, petrochemistry, nuclear industry, etc [1, 2]. They are also ideal candidates for the hot section components such as advanced gas turbine blades and aircraft engines owing to their excellent high-temperature mechanical strength, creep resistance, and enhanced grain-boundary ductility [3, 4]. However, because of their poor oxidation and hot corrosion resistance, when nickel-based superalloys are exposed to aggressive environments at elevated temperatures above 900 °C, they suffer from severe weight loss and degradation of physical properties [5, 6]. Thus, enhancing the hot corrosion resistance of nickel-based superalloys is of

significant importance. Among diverse approaches to improve the hot corrosion resistance of these materials, developing a protective coating is the most beneficial one [7, 8]. To this aim, various surface coating techniques including chemical vapor deposition (CVD) [9, 10], plasma spraying [11, 12], slurry deposition [10, 13], and hot-dipping [10, 14] have recently been employed. Amongst these methods, the pack cementation process, which is a self-generated CVD process, is the most simple and economical one [15, 16].

To synthesize high-temperature oxidation and corrosion-resistant coatings using the pack cementation technique, metallic substrates (e.g., Ni-based or Co-based superalloys, Fe-based alloys, or titanium alloys [10, 17]) are placed in a thermodynamically

semi-closed system [16] containing powders of a deposition source (e.g., Al, Si, Cr, B<sub>4</sub>C), a halide activator (e.g., NH<sub>4</sub>Cl, NH<sub>4</sub>F, MgF<sub>2</sub>, KBF<sub>4</sub>) and an inert diluent (e.g., A1<sub>2</sub>O<sub>3</sub>, SiC) [18–20]. Thus, different types of pack cementation processes including aluminizing [21–23], chromizing [24–26], siliconizing [27, 28], and boronizing [29–31] are utilized among which the first one is extensively used [19].

So far, researchers have studied the effects of coating parameters (e.g., deposition temperature and time, the activator type, pack composition, etc) on the physical properties of the pack cemented aluminide coatings including thickness, microstructure, hightemperature oxidation, and corrosion resistance [32–34]. Tong et al [32] deduced that the thickness of an aluminide coating increases parabolically with time, which indicated the domination of diffusioncontrolled growth mechanism. Xiang and Datta found that among various activators, AlCl<sub>3</sub> yielded a more uniform and thicker aluminide coating below 700 °C [34]. In addition, it has been reported that fluoride salts (e.g., NH<sub>4</sub>F) and chloride salts (e.g., NH<sub>4</sub>Cl) are generally suitable to activate the pack cementation process at high temperatures of about 1300 °C and 900 °C, respectively [16, 35]. Another study focused on the powder morphology of inert Al<sub>2</sub>O<sub>3</sub> filler and observed that the aluminide coating synthesized with spherical Al<sub>2</sub>O<sub>3</sub> possessed higher oxidation resistance than the one produced with facet  $Al_2O_3$  [33].

It is also worth mentioning that some researchers have investigated the performance of aluminide coatings by using some additive elements such as Si, Co, Pt, Cr, Ge, Hf, and Dy [36–40]. According to their results, the co-deposition of Co and Al, for example, led to an increase in the corrosion resistance of aluminide coatings [37].

Moreover, numerous research studies have pointed out the possibility of increasing the microhardness of metallic substrates using surface modification techniques. Pogrebnjak *et al* for example, employed some irradiation techniques such as high-power ion beam (HPIB) [41], high-current pulsed electron beam (HCEB) [42], and high-velocity plasma jet [43] to enhance the mechanical characteristics of the coatings including their microhardness. However, the microhardness variations across an aluminide coating synthesized by the pack cementation process have not yet been probed in detail.

Although extensive research has been conducted to improve the performance of pack cemented aluminide coatings, a detailed microstructural, topographical, and mechanical study still needs to be done to get further insights into the characteristics of aluminide coatings. Therefore, in this study, a high-activity aluminide coating is comprehensively characterized in terms of topography, roughness, microstructure, phase composition, elemental composition, and Vickers microhardness. Various analytical techniques including AFM, OM, SEM, XRD, and EDS are

employed to respond to the research questions. It was expected that the microstructural changes along the aluminide coating cross-section led to different microhardness values in the coating.

### 2. Experimental

#### 2.1. Preparation of the coating

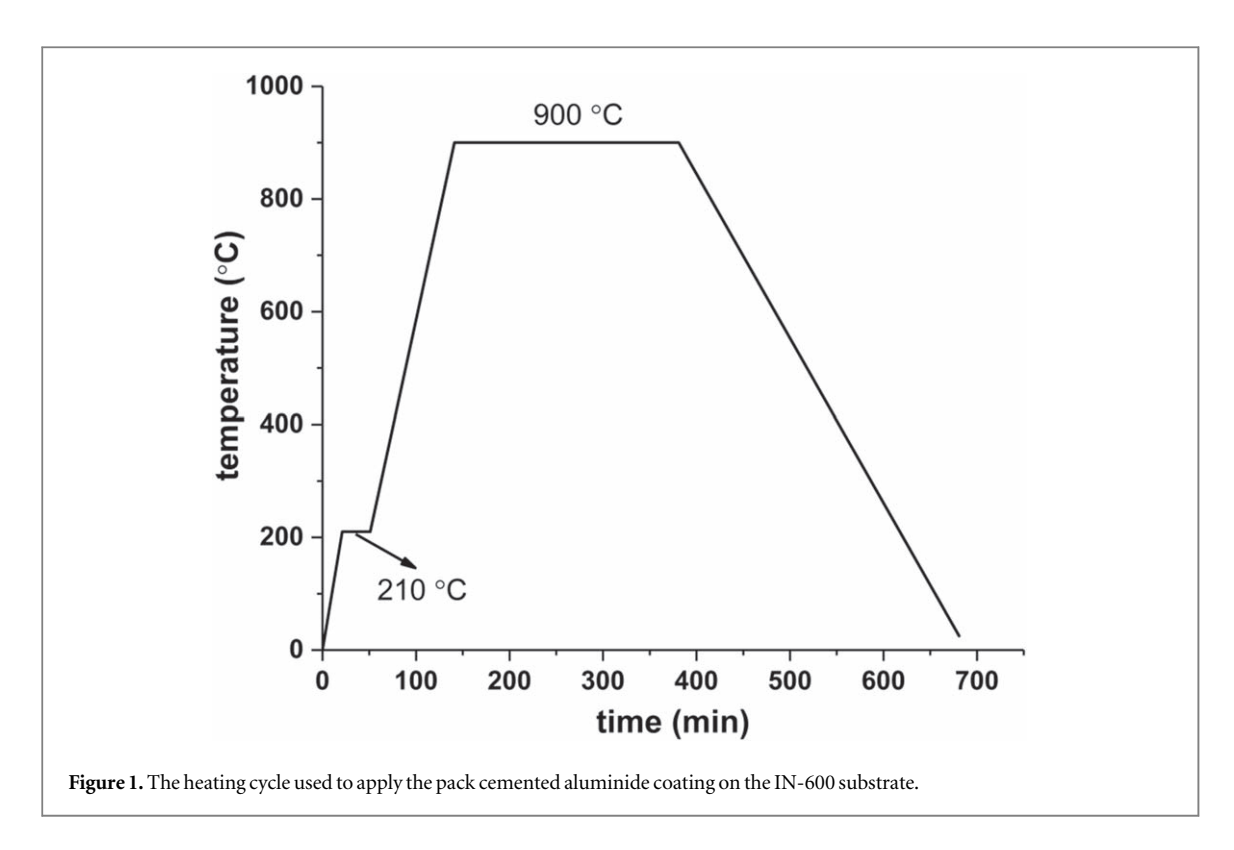
In this study, a nickel-based superalloy with the commercial name Inconel-600 (called hereafter IN-600) was used as the substrate. The chemical composition of the superalloy was 74.11Ni–15.88Cr–9.37Fe–0.28Mn–0.21Si–0.046C–0.026Cu–0.015P–0.002S (wt.%), which was analyzed using an inductively coupled plasma optical emission spectrometer (ICP-OES; Model PerkinElmer Optima 8300). Firstly, the superalloy sheet was cut to approximate dimensions of 15 mm  $\times$  15 mm  $\times$  1 mm, and all of the substrate surfaces were ground using silicon carbide abrasive paper up to 1500 grit. Then, all the substrates were ultrasonically cleaned in acetone for 5 min. Afterward, the substrates were rinsed with deionized water and dried at 37 °C.

The pack powder used for pack cementation aluminization process consisted of Al ( $<10~\mu m$  particle size, 99.5%) powder as the main deposition source, Al<sub>2</sub>O<sub>3</sub> ( $<20~\mu m$  particle size, 99.5%) powder as an inert filler, and NH<sub>4</sub>Cl (ACS reagent,  $\ge$ 99.5%) salt as an activator, which were thoroughly mixed in a mortar for 1 h. The chemical composition of the pack powder was  $18Al-80Al_2O_3-2NH_4Cl$  (wt.%). 27 g of the powder mixture was poured into an alumina crucible and the prepared IN-600 substrate was buried into the center of the crucible. The crucible was then sealed with an alumina lid and cement. It was initially cured for 1 h at room temperature and subsequently cured in an oven at 100~C for 2 h. Afterward, the prepared pack was placed in the hot zone of an alumina tube furnace.

The pack cementation process was carried out at 900 °C for 4 h with the heating rate of 10 °C·min<sup>-1</sup> and under the argon flow for protecting the substrate from oxidation during the coating formation process. The heating cycle for the coating process is also depicted in figure 1. First, the prepared pack was heated from room temperature to 210 °C within 20 min. Then, it was maintained at this temperature for 30 min to remove any humidity. Afterward, the pack was heated up to 900 °C followed by keeping at this temperature for 4 h. Finally, the pack was cooled down inside the furnace to room temperature keeping the Ar gas flowing. Finally, the samples were removed from the pack and were ultrasonically cleaned.

#### 2.2. Characterization of the coatings

Various analytical techniques were used to characterize the deposited aluminide coating. The surface topography and roughness were studied over the region of 25  $\mu$ m<sup>2</sup> for both untreated IN-600 sample



and the sample with aluminide coating using atomic force microscopy (AFM; Model Nanosurf Mobile S) equipped with Tap 190 Al-G probe. Each roughness parameter was reported as an average of eight measurements along eight different profiles. Optical microscopy (OM; Model OLYMPUS CK40M-AN) and scanning electron microscopy (SEM; Model PHENOM ProX) were utilized to study the surface morphology and the cross-sectional microstructure of the coating. Energy-dispersive spectroscopy (EDS) was employed to investigate the elemental composition variations on the surface and along the crosssection of the coating. For the cross-sectional analyses, the sample was first mounted, carefully ground with SiC abrasive papers up to 3000 grit. Then, it was polished with 1  $\mu$ m diamond slurry and degreased in the acetone bath for 5 min. Thickness measurements were performed using ImageJ software [44]. X-ray diffraction (XRD; Model BRUKER Advance-D8 x-ray diffractometer) with Cu K $_{\alpha}$  ( $\lambda = 1.5406$  Å) radiation was used to determine the phase composition of the aluminide coating in the  $2\theta$  range of  $20^{\circ}-55^{\circ}$ . The Vickers microhardness of the samples was also evaluated using an SCTMC HV-1000Z microhardness tester using a load of 100 g with a dwelling time of 15 s. Each microhardness value was reported as an average of five measurements.

#### 3. Results and discussion

The AFM 3D surface topography of the untreated IN-600 sample and the sample with deposited aluminide coating are presented in figures 2(a) and (b). It is

obvious that the surface of the untreated IN-600 sample was much smoother than the surface of the coated sample. Figure 2(c) illustrates the arithmetic average roughness ( $R_{\rm a}$ ), root-mean-squared roughness ( $R_{\rm q}$ ), maximum peak height above the mean line ( $R_{\rm p}$ ), and maximum valley depth below the mean line ( $R_{\rm v}$ ) for both of the samples. It can be seen that the formation of aluminide coating significantly increased all roughness parameters.  $R_{\rm a}$  and  $R_{\rm q}$ , for example, increased from 2.446  $\pm$  0.239 nm and 3.088  $\pm$  0.366 nm for the untreated IN-600 to 43.558  $\pm$  3.876 nm and 51.802  $\pm$  5.488 nm in the aluminide coating, respectively.

Figure 3 shows the cross-sectional microstructure of the as-formed aluminide coating. It is obvious that the coating formed on the IN-600 substrate was quite uniform without having any structural defects such as cracks, voids, and inclusions. Moreover, the coating thickness was about 198.1  $\pm$  2.5  $\mu$ m.

The phase composition of the as-formed aluminide coating is illustrated in figure 4. According to the XRD spectrum, the deposited aluminide coating was mainly composed of the intermetallic phases NiAl and Ni<sub>2</sub>Al<sub>3</sub>, which were called the major phases. The formation of these phases is attributed to the outward diffusion of Ni from the substrate and the inward diffusion of Al from the surface layer [10, 45, 46].

Figure 5 schematically illustrates the reactions occurring during the pack cementation aluminizing process. As it is observed, upon heating,  $NH_4Cl_{(s)}$  decomposes and reacts with Al powder  $(Al_{(s)})$ . As a result,  $H_{2(g)}$ ,  $HCl_{(g)}$  and a series of volatile aluminum halides (e.g.,  $AlCl_{(g)}$ ,  $AlCl_{2(g)}$ , and  $AlCl_{3(g)}$ ) are produced. Moreover, there is a zone called the 'depleted

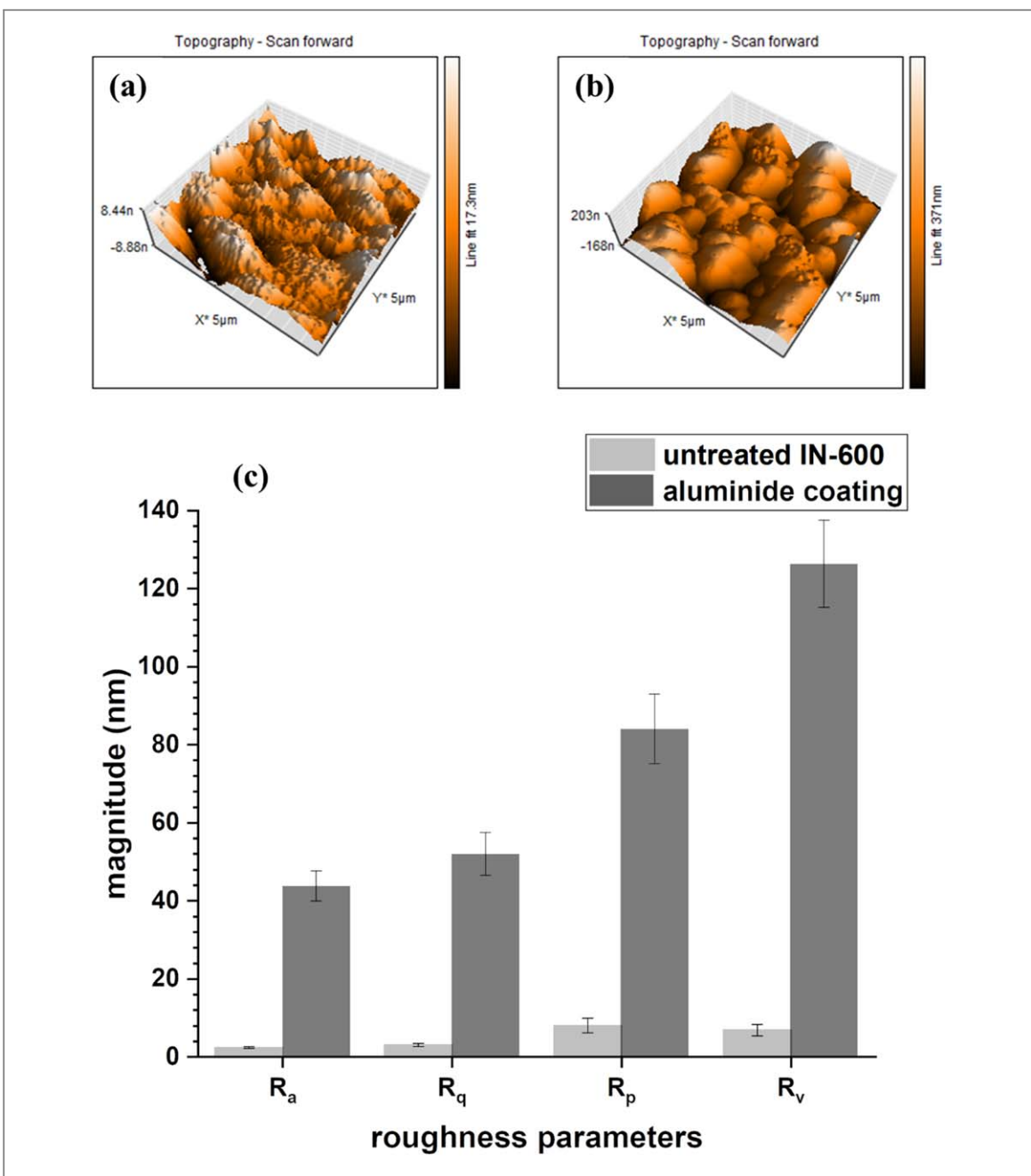


Figure 2. AFM 3D topography of (a) the untreated IN-600 sample and (b) the sample with aluminide coating; (c) roughness results for both of the samples.

zone' between the pack powder and the substrate surface. In fact, the aluminum transport into the substrate, which is due to the partial pressure gradients between the pack and the substrate surface, leads to the formation of this zone [18]. To form the aluminide coating, the volatile aluminum halides diffuse to the substrate surface through the depleted zone and release the active Al atom (indicated as [Al] in reaction (1)) [47]. Besides, since the diffusion coefficient of volatile aluminum halides increases with decreasing their molecular weight, the AlCl<sub>(g)</sub> is mainly responsible for producing the active Al atom and its transport to the substrate surface (see reaction (1)).

$$3AlCl_{(g)} \rightleftharpoons 2[Al] + AlCl_{3(g)} \tag{1}$$

Finally, the aluminide layer is formed via [Al] diffusion into the substrate. On the other hand,  $AlCl_{3(g)}$  returns to the 'undepleted pack' zone and reacts with Al powders in the pack to regenerate  $AlCl_{(g)}$  (see figure 5) [18]. Generally, the nickel aluminide  $Ni_aAl_b$  is synthesized based on the following reaction [48, 49]:

$$aNi_{(s)} + b[Al] \rightleftharpoons Ni_aAl_{b(s)} + Heat$$
 (2)

(e.g. for 
$$a = 2$$
  $b = 3 \rightarrow Ni_aAl_b = Ni_2Al_3$ )

As it can be seen in figure 4, in addition to NiAl and Ni<sub>2</sub>Al<sub>3</sub> known as major phases of the coating, there are some minor phases (i.e. Al<sub>86</sub>Cr<sub>14</sub> and Al<sub>13</sub>Fe<sub>4</sub>) precipitated because of the diffusional reactions between the produced active Al atoms and the substrate elements (e.g., Cr, Fe) [50].

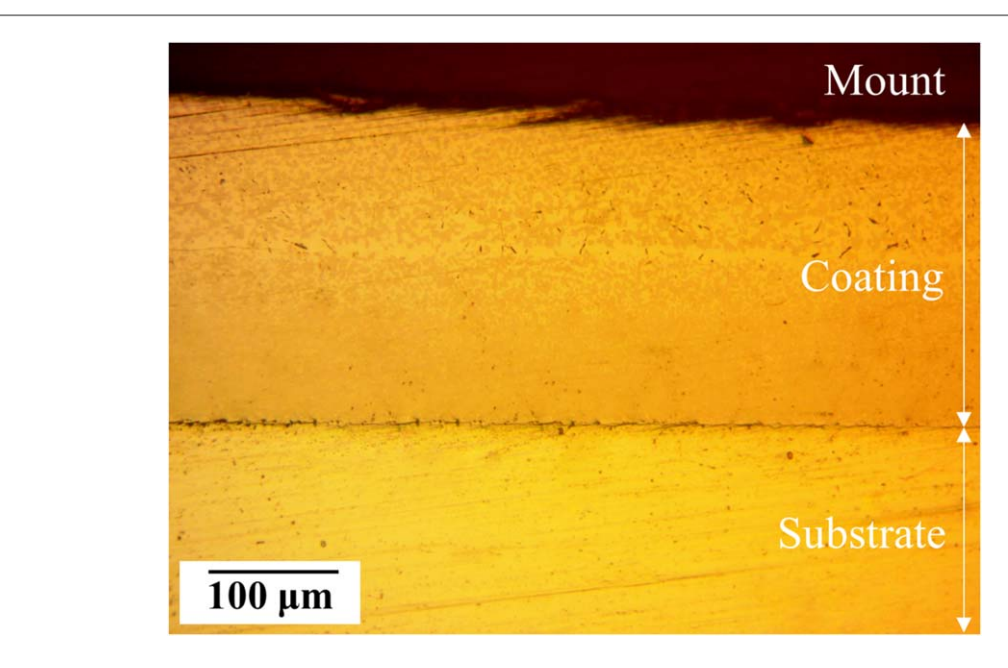
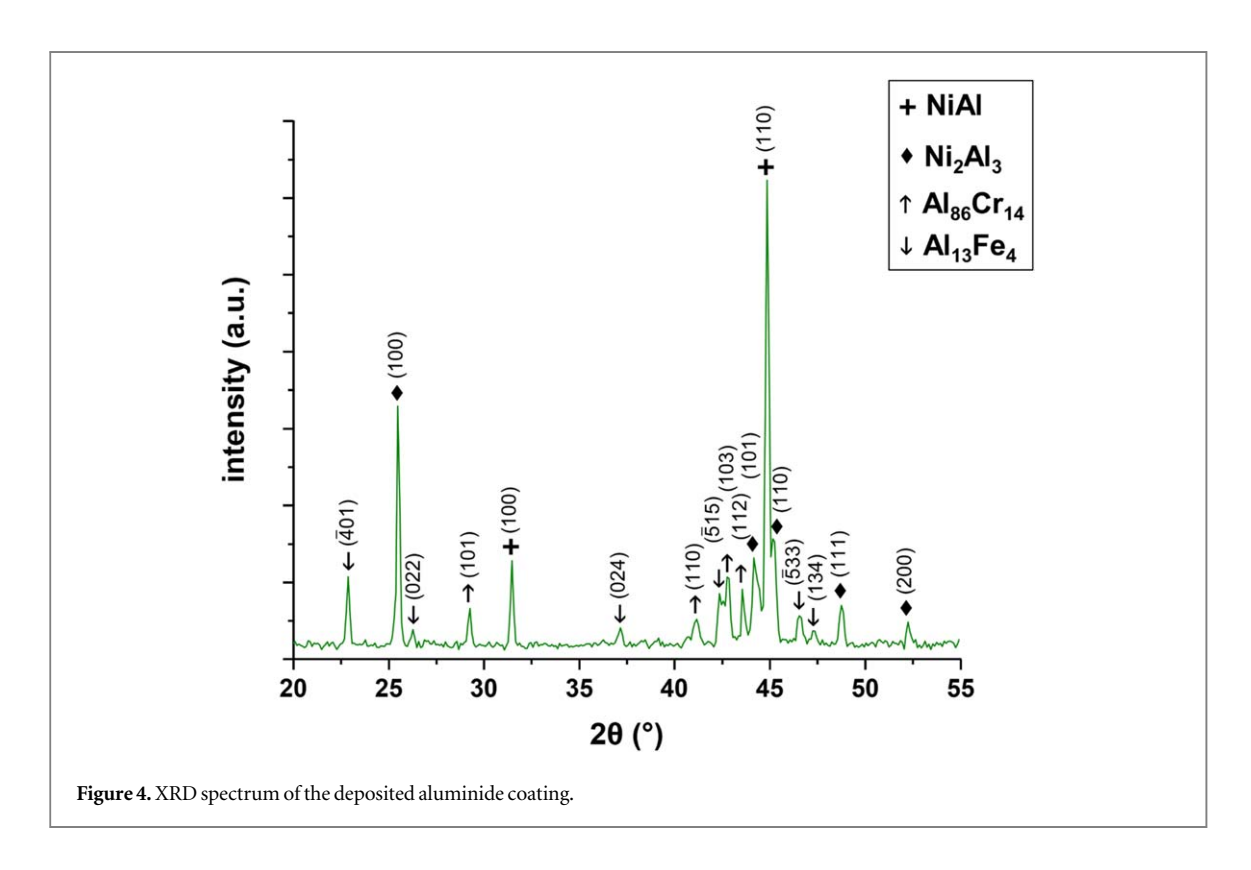


Figure 3. OM cross-sectional image of the as-formed aluminide coating.



Figures 6(a) and (b) demonstrate the surface morphology of the synthesized aluminide coating, which was evaluated using SEM. According to the results, the surface layer of the coating had a multiphase composition. As it is seen in figure 6(b), the surface of the deposited coating was not homogenous and two different areas in color (i.e., bright and dark) were detected. Based on the EDS analysis (table 1), the bright regions (spot 1) were rich in Ni whereas the dark areas (spot 2) were rich in Al.

The surface elemental mapping for the synthesized aluminide coating is shown in figure 7. As can be seen, Al, Ni, Cr, and Fe were the constituent elements of the coating and were distributed all over the surface. This is consistent with the EDS results presented in table 1. Moreover, the high amount of Al and Ni observed in this figure confirms that NiAl and Ni<sub>2</sub>Al<sub>3</sub> were the main phases of the coating (see also figure 4).

In addition to OM, the aluminide coating crosssection was characterized in detail by using SEM, which is presented in figure 8. According to figure 8,

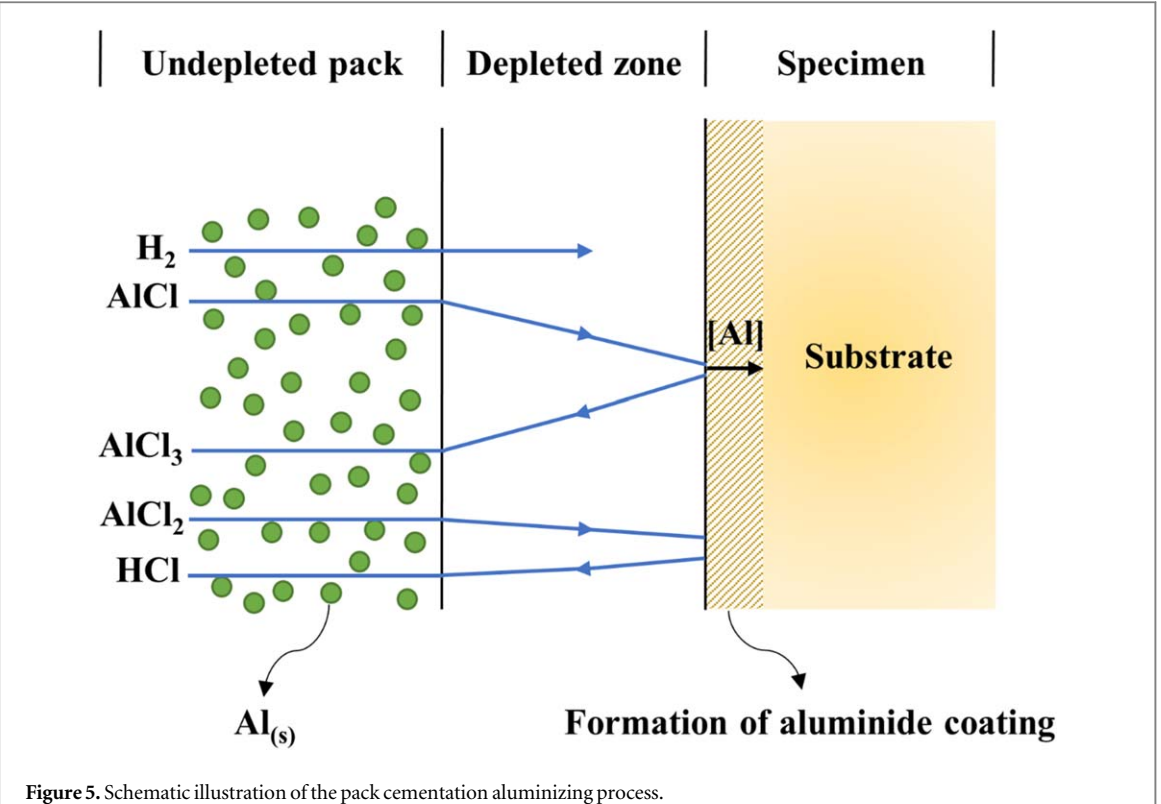


Figure 5. Schematic illustration of the pack cementation aluminizing process.

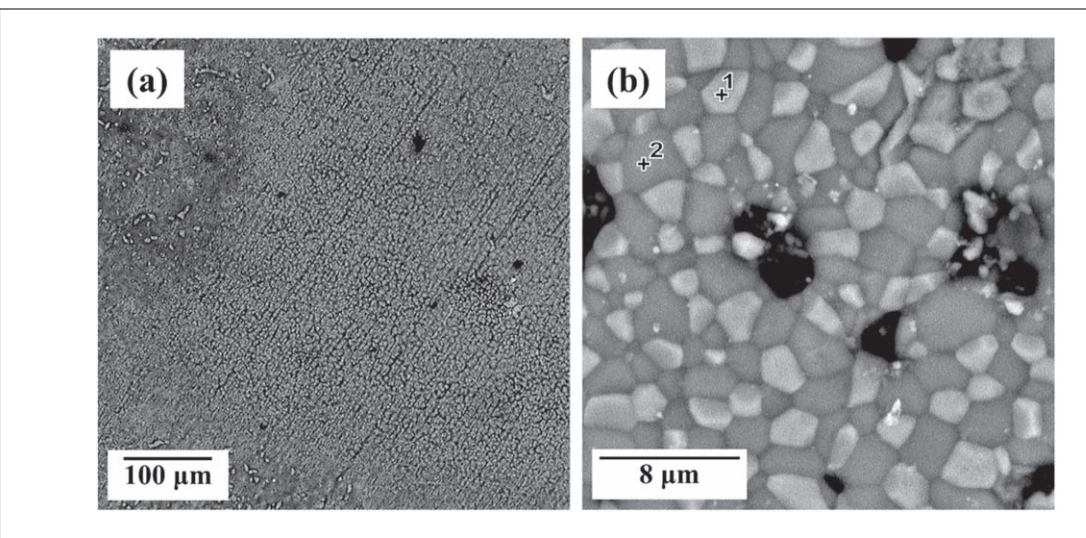


Figure 6. Surface analysis of the aluminide coating (a) low magnification BSE image; (b) high magnification BSE image.

Table 1. EDS analysis of the aluminide coating surface.

Aluminide coating surface	Region	Element (at.%)			
		Al	Ni	Cr	Fe
	Spot 1	51.1	48.9	_	_
	Spot 2	78.5	12.1	5.4	4

the deposited aluminide coating had a three-layer structure consisting of an outer layer, an inner layer, and a diffusion zone. As can be seen, the outer layer was not uniform and a significant number of black precipitates were distributed throughout this layer.

EDS analysis of the outer layer (table 2) indicates that the greyish areas were rich in Ni whilst the black precipitates were mainly an Al-rich phase. Considering the XRD spectrum of the coating and the EDS analysis (see figure 4 and table 2), the greyish regions (spot 1) and the black precipitates (spot 2) were mainly the heavy phase NiAl, and the light phase Ni<sub>2</sub>Al<sub>3</sub>, respectively. However, according to figure 8, the inner layer was quite homogenous with a negligible content of black precipitates indicating the presence of NiAl in this layer.

The pack cementation process was carried out at a relatively low temperature (i.e., 900 °C) with high Al

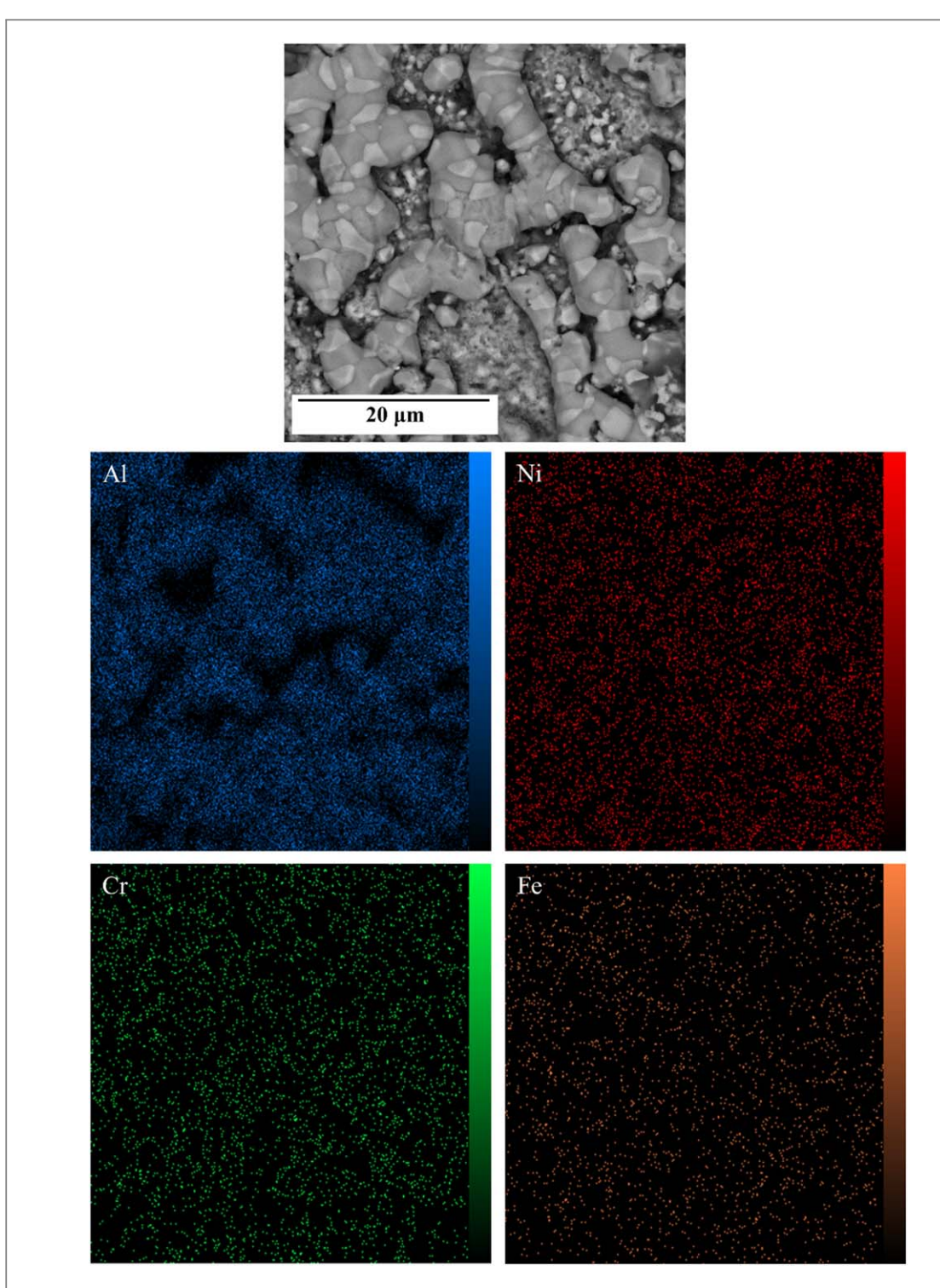


Figure 7. EDS elemental mapping for the aluminide coating surface.

activity in the pack (18 wt. % Al in the pack). As a result, the aluminide coating in this study was synthesized predominantly via inward Al diffusion [10]. On the other hand, as it is observed in figure 8, there is a narrow diffusion zone under the inner layer, which confirms the limited occurrence of outward Ni diffusion [17, 45, 51].

Figure 9 illustrates the elemental depth profile across the synthesized aluminide coating. According to figure 9(b), by moving from the surface of the aluminide coating down to its diffusion zone, the

concentration of Al fell gradually from 73.8  $\pm$  3.5 at. % to 45.1  $\pm$  2.4 at.%. However, it dropped sharply to 4.6  $\pm$  1.8 at.% by moving toward the substrate. The atomic percent of Ni, on the other hand, increased moderately from 20.3  $\pm$  2.6 at.% in the surface layer to 32.3  $\pm$  2.9 at.% in the diffusion zone but increased dramatically to 72.3  $\pm$  2.1 at.% in the substrate. Additionally, there was a slight increase in the amount of Cr from 3.8  $\pm$  2.9 at.% in the top surface to 10.1  $\pm$  3.7 at.% in the coating inner layer followed by a steep rise to 18.1  $\pm$  2.2 at.% in the diffusion zone. However,

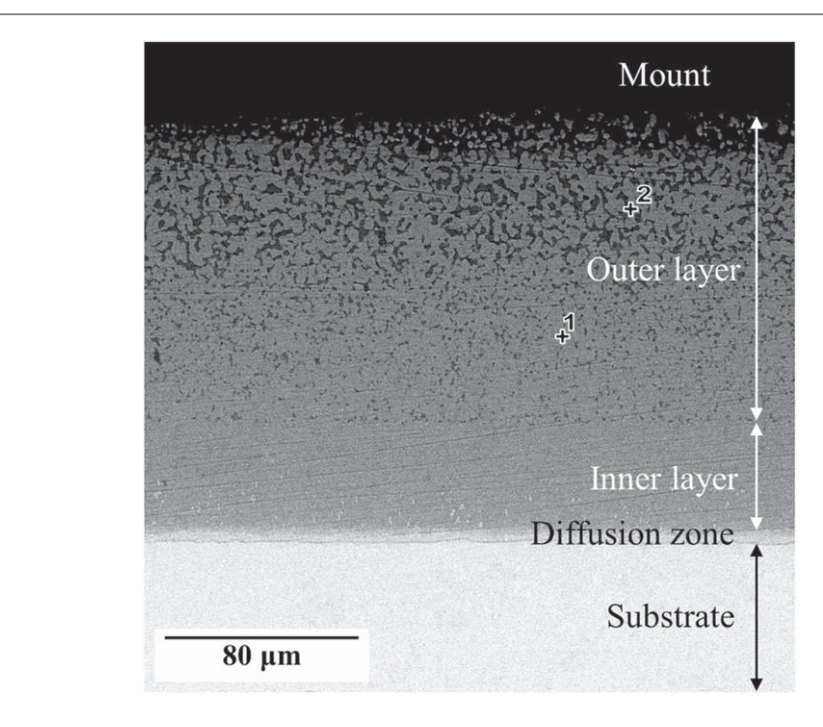


Figure 8. Cross-sectional BSE image of the aluminide coating.

**Table 2.** EDS analysis of the aluminide coating outer layer.

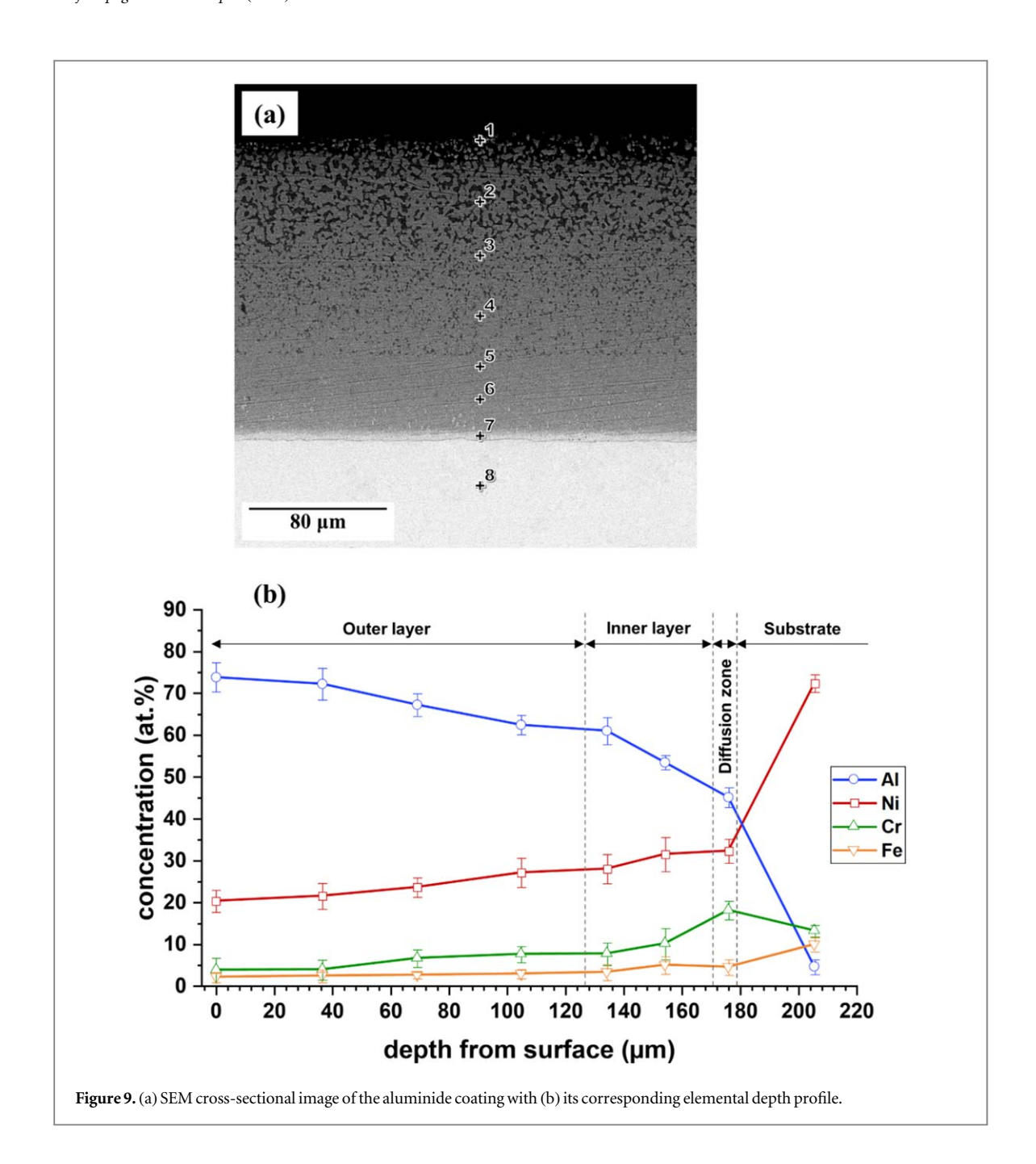
Aluminide coating outer layer		]	Element (at.%)			
	Region	Al	Ni	Cr	Fe	
	Spot 1 Spot 2	50.6 69	49.4 20.8	— 7.3		

after peaking in this layer, the corresponding value fell moderately to 13.2  $\pm$  1.4 at.% in the substrate. Moreover, a peak in the Cr concentration in the diffusion zone was attributed to the limited solubility of this element in Al [52], which led to a low diffusion rate of Cr in the inner layer of the produced aluminide coating. Subsequently, Cr atoms accumulated and thus a Crrich phase was formed at the coating/substrate interface. Finally, the content of Fe increased continually from 2.1  $\pm$  1.2 at.% in the surface layer to 9.9  $\pm$  1.7 at.% in the substrate. Moreover, as can be observed in figure 9(b), the calculated uncertainties and thus the plotted error bars were small in the substrate profile, which was due to the almost uniform microstructure and the elemental distribution across the substrate. However, the produced coating was not as homogeneous as the substrate in terms of phase composition. In other words, there were four different phases present across the aluminide coating (i.e., NiAl, Ni<sub>2</sub>Al<sub>3</sub>, Al<sub>86</sub>Cr<sub>14</sub>, and Al<sub>13</sub>Fe<sub>4</sub>) which caused different elemental distributions throughout the coating. Thus, bigger error bars were observed in the coating profile compared to the substrate one.

Figure 10 illustrates the elemental mapping analysis image obtained from the cross-section of the

produced aluminide coating. According to this figure, Al was just distributed across the produced aluminide coating. In contrast, Ni was detected in the cross-section of both the substrate and coating, demonstrating the outward diffusion of Ni from the IN-600 substrate toward the surface of the applied coating. Moreover, the presence of a low amount of Cr and Fe in the coating region originated from the substrate. Here, it is worth noting that a thin Cr rich layer was observed at the substrate/coating interface which confirms the accumulation of this element in the diffusion zone and is in accordance with the plotted elemental depth profile (see figure 9(b)).

The EDS line scan analysis was also carried out to get further insight into the concentration variations of the elements across the produced aluminide coating. Figure 11 reveals that the Al signal was at its highest level in the outer layer (near the surface) of the coating, but due to the inward Al diffusion, the corresponding signal intensity decreased moderately in the inner layer, and then dropped dramatically at the coating/ substrate interface (diffusion zone). This is consistent with the measured concentration profile for Al (see figure 9(b)). In contrast, because of the outward Ni diffusion from the substrate to the surface of the coating, the Ni signal increased slightly from the outer layer towards the inner layer followed by a sharp rise in the diffusion zone and the substrate. Moreover, a little amount of Cr and Fe were detected in the coating illustrating the outward diffusion of the substrate alloying elements as well. Although the amount of Cr in the formed coating was lower than Ni and Al, an intense Cr signal was observed at the depth of about 200  $\mu$ m from the surface of the coating confirming the



accumulation of this element in the diffusion zone. A higher Cr signal was also detected in the substrate than across the coating. Similar trends in elemental composition variations were reported by Bai *et al* [19].

As it was observed in figure 8, the microstructure changed along the aluminide coating thickness. Hence, Vickers microhardness measurements were conducted on different coating layers in order to provide more precise microhardness data from the coating. According to figure 12, the microhardness of the substrate was about  $185.6 \pm 15.8$  Hv. However, applying the aluminide coating significantly increased the microhardness. Due to containing the hard precipitates of MC and  $M_{23}C_6$  carbides and the Cr-rich sigma phase,  $\sigma$ -(Cr, Al), in a  $\beta$ -(NiA1) matrix [10], the coating diffusion zone possessed the highest Vickers microhardness of about  $1130.4 \pm 42.5$  Hv. It is

noteworthy that the average microhardness of the coating outer layer was lower than that of the inner layer (863.9  $\pm$  102.6 Hv versus 928.9  $\pm$  32.8 Hv). Moreover, it can be seen that a relatively high error bar is shown for the outer layer of the coating, which was related to the presence of two different phases (i.e., NiAl and Ni<sub>2</sub>Al<sub>3</sub>) throughout the outer layer (see figure 8). In other words, a high microhardness value of about 959.7 Hv was measured in the NiAl regions whilst in the areas where Ni<sub>2</sub>Al<sub>3</sub> was present, a relatively low microhardness value of about 733.5 Hv was reported. However, this issue did not occur in the coating inner layer due to the fact that it was uniform and mainly composed of NiAl (see figure 8).

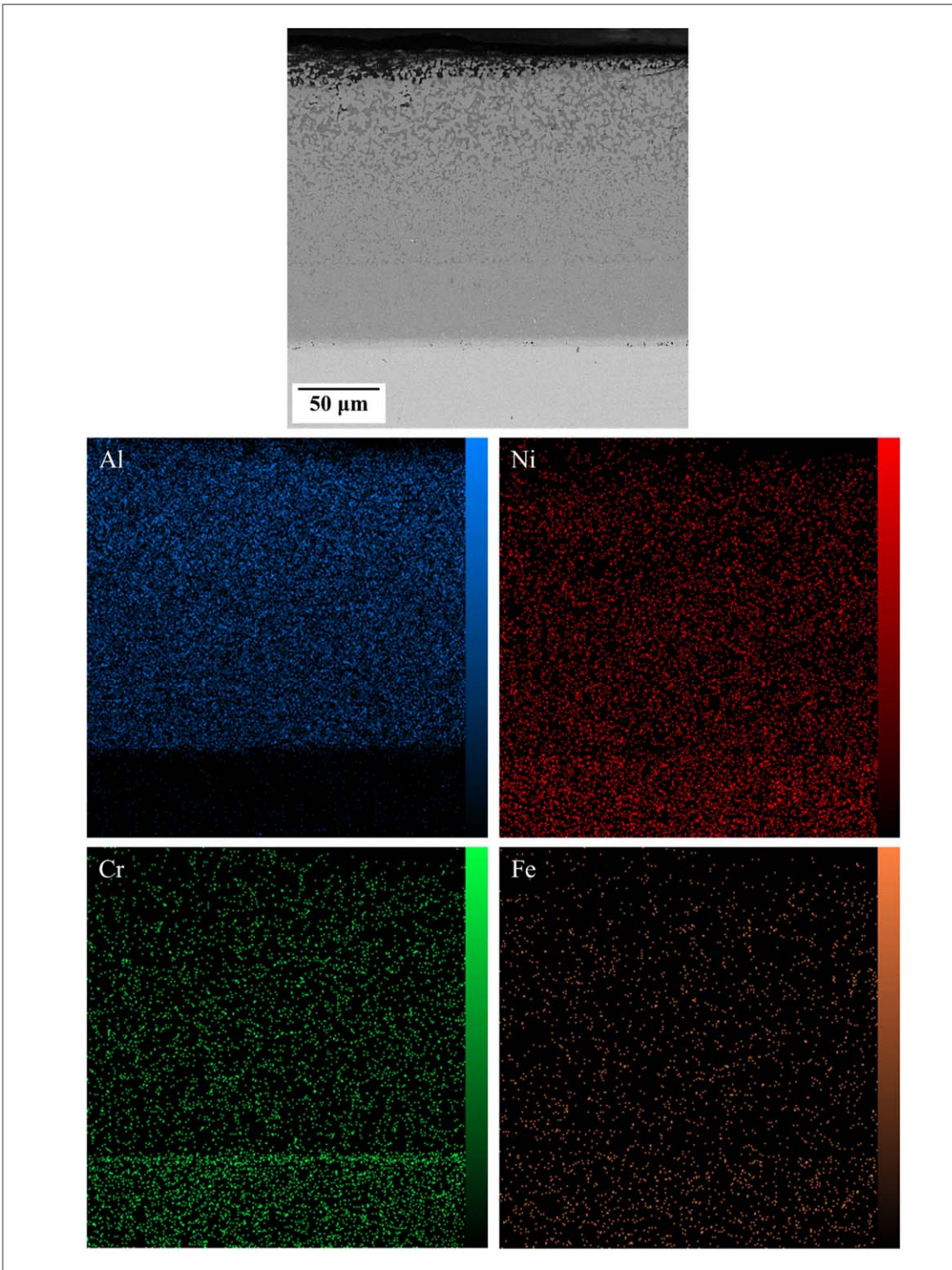
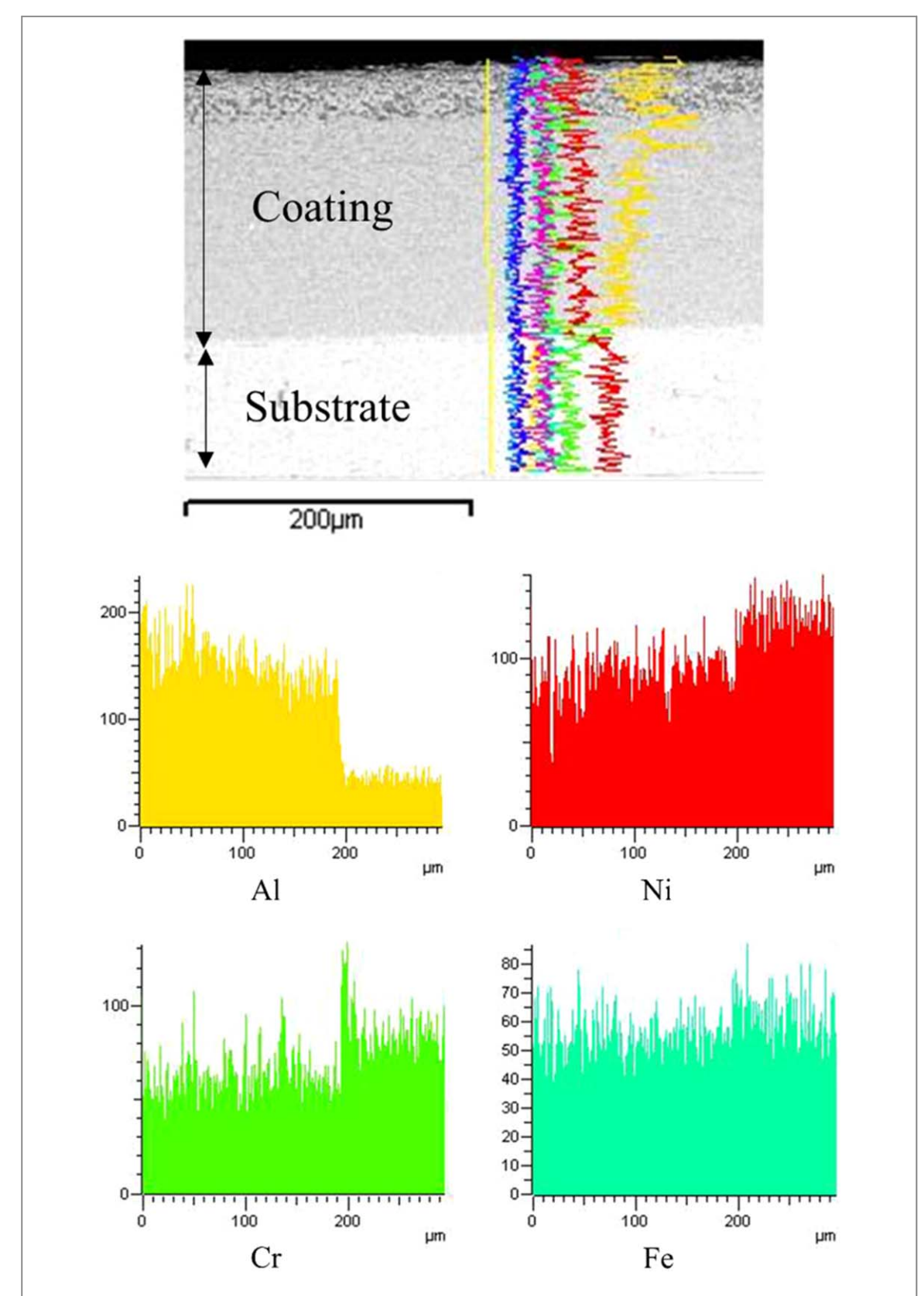


Figure 10. EDS elemental mapping for the aluminide coating cross-section.

#### 4. Conclusions

Using the pack composition of 18Al–80Al<sub>2</sub>O<sub>3</sub>–2NH<sub>4</sub>Cl (wt.%), the aluminide diffusion coating was successfully deposited on the substrate of Inconel-600. The coating had a three-layer structure consisting of 'the outer layer', 'the inner layer' and 'the diffusion zone'. The cross-sectional microstructure confirmed that the aluminide coating was synthesized mainly via the inward diffusion of Al with the limited occurrence of the outward Ni

diffusion. The XRD analysis detected the NiAl and  $Ni_2Al_3$  phases as the main constituents of the coating, which were formed as a result of the mutual Al and Ni diffusion. The Vickers microhardness results demonstrated a significant increase in the microhardness of the sample after applying the aluminide coating. They also illustrated that the microhardness varied along the coating thickness due to microstructural changes. The highest microhardness was reported for the diffusion zone of the coating with the average amount

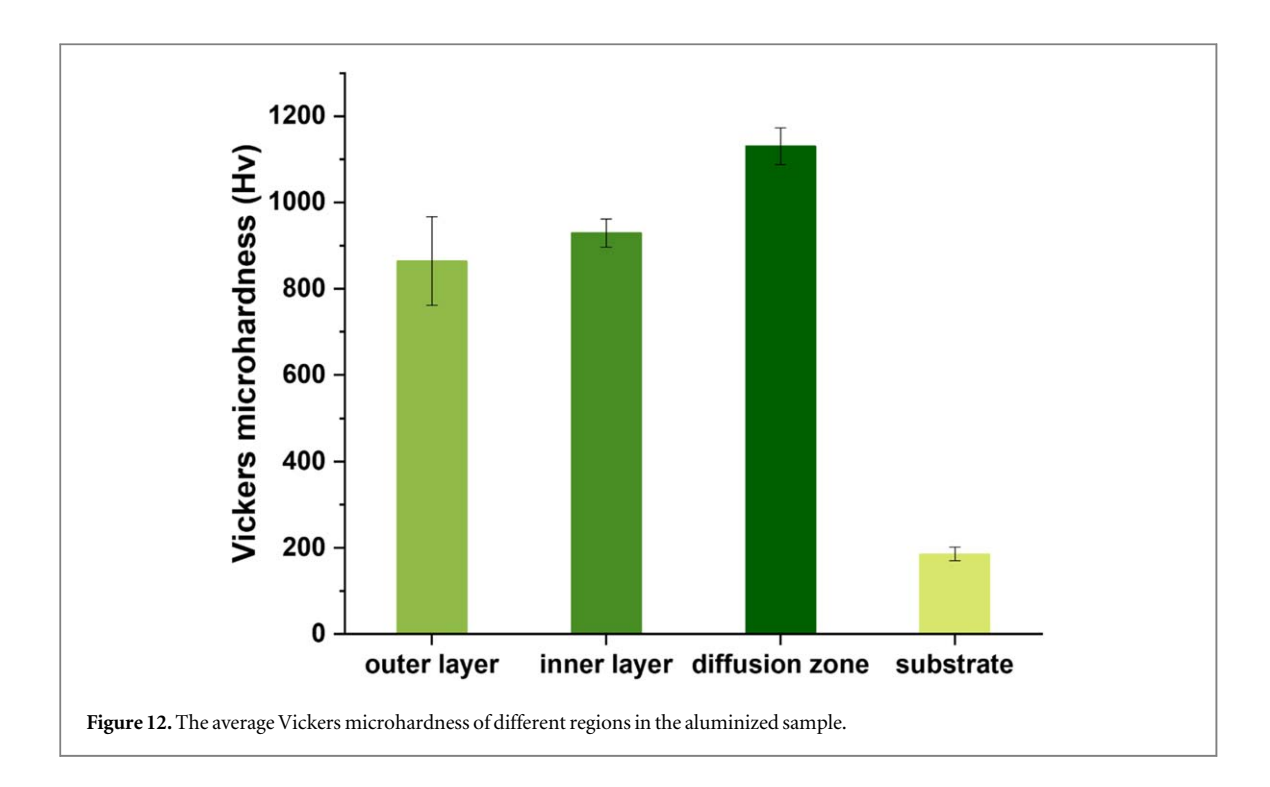


**Figure 11.** EDS line scan analysis from the cross-section of the produced aluminide coating; note that the X-axis represents the depth from the coating surface in  $\mu$ m and Y-axis is the signal intensity in an arbitrary unit.

of 1130.4  $\pm$  42.5 Hv, which was due to the presence of hard carbide precipitates and sigma phase in this layer.

## Data availability statement

The data that support the findings of this study are available upon reasonable request from the authors.



#### **ORCID** iDs

Sina Mahini https://orcid.org/0000-0002-5375-0521

Shahin Khameneh Asl https://orcid.org/0000-0002-6979-0376

Taher Rabizadeh https://orcid.org/0000-0003-3483-2764

Hossein Aghajani https://orcid.org/0000-0002-7866-8807

#### References

- Yin Z F, Zhao W Z, Lai W Y and Zhao X H 2009
  Electrochemical behaviour of Ni-base alloys exposed under oil/gas field environments Corros. Sci. 51 1702–6
- [2] Baidridge T, Poling G, Foroozmehr E, Kovacevic R, Metz T, Kadekar V and Gupta M C 2013 Laser cladding of Inconel 690 on Inconel 600 superalloy for corrosion protection in nuclear applications Opt. Lasers Eng. 51 180—4
- [3] Campbell F C 2006 Superalloys Manufacturing Technology for Aerospace Structural Materials (Amsterdam: Elsevier) pp 211–72
- [4] Seth B B 2000 Superalloys: the utility gas turbine Perspective Superalloys 2000 (Ninth International Symposium) (Warrendale, Pennsylvania: The Minerals, Metals & Materials Society (TMS)) pp 3–16
- [5] Gupta A K, Immarigeon J P and Patnaik P C 1989 Review of factors controlling the gas turbine hot section environment and their influence on hot salt corrosion test methods *High Temp. Technol.* 7 173–86
- [6] Goebel J A, Pettit F S and Goward G W 1973 Mechanisms for the hot corrosion of nickel-base alloys Metall. Trans. 4 261–78
- [7] Wang F, Lou H, Bai L and Wu W 1989 High Temperature Corrosion 2 ed R Streiff et al 1989 (Barking, UK: Elseveier Science Publ.) pp 387–9 Wang F, Lou H, Bai L and Wu W 1989 Mat. Sci. Eng. A 121 387–9
- [8] Goward GW 1998 Progress in coatings for gas turbine airfoils Surf. Coatings Technol. 108–109 73–9

- [9] Müller J, Schierling M, Zimmermann E and Neuschütz D 1999 Chemical vapor deposition of smooth α-Al<sub>2</sub>O<sub>3</sub> films on nickel base superalloys as diffusion barriers Surf. Coat. Technol. 120–121 16–21
- [10] Patnaik P C 1989 Intermetallic coatings for high temperature applications—a review Mater. Manuf. Process. 4 133–52
- [11] Degout D, Kassabji F and Fauchais P 1984 Titanium dioxide plasma treatment Plasma Chem. Plasma Process. 4 179–98
- [12] Haynes J A, Rigney E D, Ferber M K and Porter W D 1996 Oxidation and degradation of a plasma-sprayed thermal barrier coating system Surf. Coatings Technol. 86–87 102–8
- [13] Triani R M, Gomes L F D A, Aureliano R J T, Neto A L, Totten G E and Casteletti L C 2020 Production of aluminide layers on AISI 304 stainless steel at low temperatures using the slurry process J. Mater. Eng. Perform. 29 3568–74
- [14] Chen Y Y, Lin C B and Mei C C 2019 The influence of nickel additions to liquid A359 on hot-dip aluminizing of solid S45C steel J. Mater. Eng. Perform. 28 5195–206
- [15] Mévrel R, Duret C and Pichoir R 1986 Pack cementation processes Mater. Sci. Technol. (United Kingdom) 2 201–6
- [16] Kung S C and Rapp R A 1988 Kinetic study of aluminization of iron by using the pack cementation technique J. Electrochem. Soc. 135 731–41
- [17] Xiang Z D, Burnell-Gray J S and Datta P K 2001 Conditions for codeposition of Al and Cr on Ni base superalloys by pack cementation process Surf. Eng. 17 287–94
- [18] Meyers B and Lynn S 1994 ASM Handbook Volume 5: Surface Engineering (Materials Park, OH: ASM International)
- [19] Bai C Y, Luo Y J and Koo C H 2004 Improvement of high temperature oxidation and corrosion resistance of superalloy IN-738LC by pack cementation Surf. Coatings Technol. 183 74–88
- [20] Murakami T, Matsuzaki K, Gomi Y, Sasaki S and Inui H 2013 Microstructure and tribological properties of gray cast iron specimens coated by aluminizing, boronizing, chromizing and siliconizing Mater. Res. Soc. Symp. Proc. 1516 115–20
- [21] Sun Y, Dong J, Zhao P and Dou B 2017 Formation and phase transformation of aluminide coating prepared by lowtemperature aluminizing process Surf. Coatings Technol. 330 234–40
- [22] Khalid F A, Hussain N and Qureshi A H 2002 Microstructural study on oxidation of aluminized coating on inconel 625 J. Mater. Eng. Perform. 11 211–4

- [23] Gheisari R, Bashandeh K and Polycarpou A A 2019 Effect of surface polishing on the tribological performance of hard coatings under lubricated three-body abrasive conditions Surf. Topogr.: Metrol. Prop. 7 045001
- [24] Ping J, Cui X, Pu J, Jiang X, Zhang X and Zhong Y 2020 Structural, tribological and corrosion properties of plasma nitrided-chromized-316L stainless steel in air and artificial seawater Surf. Topogr.: Metrol. Prop. 8 015005
- [25] Zhou Y B, Chen H, Zhang H and Wang Y 2008 Preparation and oxidation of an Y<sub>2</sub>O<sub>3</sub>-dispersed chromizing coating by pack cementation at 800 °C Vacuum 82 748–53
- [26] Lu J, Yang Z, Zhang B, Huang J and Xu H 2018 Corrosion behavior of candidate materials used for urea hydrolysis equipment in coal-fired selective catalytic reduction units J. Mater. Eng. Perform. 27 3290–6
- [27] Swadźba R 2019 High temperature oxidation behavior of C103 alloy with boronized and siliconized coatings during 1000 h at 1100 °C in air Surf. Coatings Technol. 370 331–9
- [28] Mitoraj-Królikowska M and Godlewska E 2018 Silicide coatings on Ti-6Al-1Mn (at.%) alloy and their oxidation resistance *Surf. Coatings Technol.* 334 491–9
- [29] Raghs H A, Kondul B and Cetin M H 2020 Investigation of wear behavior of boronized H13 steel under environment of nano-silver-added lubricants coated with different ligands Surf. Topogr.: Metrol. Prop. 8 015007
- [30] Anthymidis K G, Maragoudakis N, Stergioudis G, Haidar O and Tsipas D N 2003 A comparative study of boride coatings obtained by pack cementation method and by fluidized bed technology *Mater. Lett.* 57 2399–403
- [31] Qian L L and Stone G A 1995 A study of the behavior of boron diffusion in plain carbon steels J. Mater. Eng. Perform. 4 59–62
- [32] Tong L, Dengzun Y and Chungen Z 2010 Low-temperature formation of aluminide coatings on Ni-base superalloys by pack cementation *Process Chinese J. Aeronaut.* 23 381–5
- [33] Mohammadi K and Haghi A K 2008 A study on characterization of pack-cemented aluminide coating on metals J. Mater. Process. Technol. 201 669–72
- [34] Xiang Z D and Datta P K 2006 Relationship between pack chemistry and aluminide coating formation for lowtemperature aluminisation of alloy steels Acta Mater. 54 4453–63
- [35] Kipkemoi J and Tsipas D 1996 Rare-earth modified chromium-aluminide coatings applied by pack cementation method on low-alloy steels J. Mater. Sci. 31 6247–50
- [36] Haynes J A, Pint B A, More K L, Zhang Y and Wright I G 2002 Influence of sulfur, platinum, and hafnium on the oxidation behavior of CVD NiAl bond coatings Oxid. Met. 58 513–44
- [37] Qiao M and Zhou C 2012 Hot corrosion behavior of Co modified NiAl coating on nickel base superalloys Corros. Sci. 63 239–45
- [38] Volovitch P, Masse J E, Fabre A, Barrallier L and Saikaly W 2008 Microstructure and corrosion resistance of magnesium

- alloy ZE41 with laser surface cladding by Al–Si powder *Surf. Coatings Technol.* **202** 4901–14
- [39] Azarmehr S A, Shirvani K, Solimani A, Schütze M and Galetz M C 2019 Effects of Pt and Si on the low temperature hot corrosion of aluminide coatings exposed to Na<sub>2</sub>SO<sub>4</sub> -60 mol% V<sub>2</sub>O<sub>5</sub> salt Surf. Coatings Technol. 362 252-61
- [40] Galetz M C, Oskay C and Madloch S 2019 Microstructural degradation and interdiffusion behavior of NiAl and Gemodified NiAl coatings deposited on alloy 602 CA Surf. Coatings Technol. 364 211–7
- [41] Pogrebnjak A D and Ruzimov S M 1987 Increased microhardness and positron annihilation in Al exposed to a high-power ion beam Phys. Lett. A 120 259–61
- [42] Pogrebnjak A D and Shumakova N I 1999 Effect of 'duplex' treatment on changes of physical and mechanical properties of steel (0.3 wt% C) Surf. Coatings Technol. 122 183–7
- [43] Pogrebnjak A D, Ruzimov S M, Alontseva D L, Zukowski P, Karwat C, Kozak C and Kolasik M 2007 Structure and properties of coatings on Ni base deposited using a plasma jet before and after electron a beam irradiation *Vacuum* 81 1243–51
- [44] Rueden C T, Schindelin J, Hiner M C, DeZonia B E, Walter A E, Arena E T and Eliceiri K W 2017 ImageJ2: ImageJ for the next generation of scientific image data *BMC Bioinf*.
- [45] Goward GW and Boone DH 1971 Mechanisms of formation of diffusion aluminide coatings on nickel-base superalloys Oxid. Met. 3 475–95
- [46] Das O K, Singh V and Joshi S V 1998 Evolution of aluminide coating microstructure on nickel-base cast superalloy CM-247 in a single-step high-activity aluminizing process *Metall. Mater. Trans. A Phys. Metall. Mater. Sci.* 29 2173–88
- [47] Fu C, Kong W K and Cao G H 2014 Microstructure and oxidation behavior of Al+Si co-deposited coatings on nickelbased superalloys Surf. Coatings Technol. 258 347–52
- [48] Fu C, Wang C H, Ren Z M and Cao G H 2015 Comparison of microstructure and oxidation behavior between Pt-free and Pt-modified δ-Ni<sub>2</sub>Si coatings on Ni-based superalloys Corros. Sci. 98 211–22
- [49] Morsi K 2001 Review: reaction synthesis processing of Ni–Al intermetallic materials *Mater. Sci. Eng.* A 299 1-15
- [50] Zhou F, Gao M, Tu G F, Liu K and Pengu K W 2014 Aluminide coating prepared on Ni-base superalloy by pack cementation Advanced Materials Research 848 11–7
- [51] Xiang Z D, Burnell-Gray J S and Datta P K 2001 Aluminide coating formation on nickel-base superalloys by pack cementation process J. Mater. Sci. 36 5673–82
- [52] Massalski T B, Okamoto H (Hiroaki) and ASM International 1990 Binary Alloy Phase Diagrams (Materials Park, OH: ASM International)